Astron. Astrophys. 360, 562–574 (2000)

ASTRONOMY AND ASTROPHYSICS

CO_2 emission in EP Aqr: Probing the extended atmosphere⋆

J. Cami[1,2], I. Yamamura[1], T. de Jong[3,1], A.G.G.M. Tielens[2,4], K. Justtanont[5], and L.B.F.M. Waters[1,2]

[1] Astronomical Institute "Anton Pannekoek", University of Amsterdam, Kruislaan 403, 1098 SJ Amsterdam, The Netherlands
[2] SRON-Groningen, P.O. Box 800, 9700 AV Groningen, The Netherlands
[3] SRON, Sorbonnelaan 2, 3584 CA Utrecht, The Netherlands
[4] Kapteyn Institute, P.O. Box 800, 9700 AV Groningen, The Netherlands
[5] Stockholm Observatory, 13336 Saltsjöbaden, Sweden

Received 24 February 2000 / Accepted 7 June 2000

Abstract. We present an analysis of the ISO/SWS full resolution scan between 12.5 and 16.5 μm of the O-rich AGB star EP Aqr, exhibiting a number of strong CO_2 emission bands. We have developed a simple LTE model to calculate theoretical CO_2 spectra assuming a single-layer slab geometry and compared the SWS observations to this model in order to infer the physical properties of the extended atmosphere. The single layer slab model is able to reproduce the individual band profiles quite well with optically thick bands (column densities typically $10^{18.5}$ cm^{-2}). The derived excitation temperatures for the different bands are in the range $T \sim 350-700$ K in a region which extends from $\sim 4-9R_*$. The fundamental CO_2 bending mode at 14.98 μm furthermore shows evidence for an optically thin component arising from a much cooler ($T \sim 100$ K) and more extended ($R_{\rm em} \sim 100R_*$) layer. The strong spectral signature of $^{13}CO_2$ in the spectrum allows an (uncertain) determination of the $^{12}C/^{13}C$ ratio ~ 10. The parameters derived for the CO_2 bands allow us to estimate the local temperature and density structure of the extended atmosphere. We find that the derived local gas temperatures are somewhat lower than predicted by hydrodynamical model calculations whereas the local gas densities are in good agreement with these models when using CO_2 abundances derived from chemical network calculations. The CO_2 layer extends from close to the stellar photosphere to the inner part of the dust forming region which makes it a unique new probe of the whole extended atmosphere and the region where dust formation takes place.

Key words: stars: AGB and post-AGB – stars: circumstellar matter – stars: individual: EP Aqr – stars: late-type – stars: winds, outflows – infrared: stars

1. Introduction

When low- and intermediate-mass stars evolve up the Asymptotic Giant Branch (AGB), they undergo substantial mass loss which determines their evolution in this phase. A complex chemistry - based on either carbon or oxygen preponderance - is initiated in the outflow leading to the formation of molecules and dust which are then dispersed in the interstellar medium. AGB stars are believed to be the main factories of interstellar dust and contribute significantly to the chemical enrichment of the gas of the galaxy. Although the analysis of observational data and the results of hydrodynamical model atmosphere calculations in recent years has greatly improved our knowledge on some topics, the mass loss mechanism is still not well understood. The way pulsation and dust formation affects the mass loss remains the subject of debate.

Observations with the ISO/SWS Kessler et al. 1996, de Graauw et al. 1996 have revealed the presence of numerous molecules in the outflows of AGB stars (Tsuji et al. 1997; Justtanont et al. 1998; Yamamura et al. 1999a,b). The excitation temperatures of these molecules and their typical distances to the central star suggest that the observed bands of different molecules are formed in slightly different regions : an "extended atmosphere".

As the "extended atmosphere" is extending from the stellar photosphere to the inner part of the dusty circumstellar material that is generally believed to drive the strong AGB mass loss, studying the physical properties of this region allows us to find the missing link between stellar pulsations and the *physical* processes of dust formation and wind acceleration in the outflow. The infrared molecular bands are excellent probes to study the physical conditions in the region of the most recent mass loss. Moreover, the very presence of these molecules may shed some light on the *chemical* pathways to dust formation.

Justtanont et al. (1998) and Ryde et al. (1998) independently reported the discovery with the ISO-SWS of ro-vibrational emission bands of CO_2 between 13 and 17 μm, observed in the spectra of O-rich AGB stars that also exhibit the 13 μm dust feature.

By comparing the observations with optically thin LTE models, Justtanont et al. (1998) and Cami et al. (1997) concluded

Send offprint requests to: J. Cami, (cami@astro.rug.nl)

⋆ Based on observations with ISO, an ESA project with instruments funded by ESA Member States (especially the PI countries: France, Germany, the Netherlands and the United Kingdom) with the participation of ISAS and NASA. The SWS is a joint project of SRON and MPE.

that the excitation temperature of the observed CO_2 emission bands is of the order of 650 K and that the emitting CO_2 layer is probably located at a few stellar radii. The optically thin LTE model is able to reproduce the observed Q-branch band profiles very well with a single temperature, but not the relative band intensities. Especially the fundamental bending mode at 15 μm is always weaker than expected from optically thin LTE models that fit the other CO_2 bands; the 15 μm band is sometimes even seen in absorption.

Ryde et al. (1999) suggest that this is due to non-LTE effects. Estimating that the bands are optically thin, they argue that the density in the CO_2 emitting region is probably well over the critical density for thermalizing the *rotational* levels - which determines the band width - but lower than the critical density for thermalizing the *vibrational* levels - which determines the relative strengths of the bands. This would explain why an optically thin LTE model can reproduce the individual bands with a single temperature but not the relative band intensities. However, even in an optically thin non-LTE situation, the relative intensities of the P-, Q- and R- branch bands originating from the same vibrational level are only determined by their relative Einstein A coefficients; therefore the relative intensities of these bands should be the same as for an LTE model - which is not the case for the observed bands. This suggests that the Q-branch bands may well be optically thick.

Gonzalez-Alfonso & Cernicharo (1999) present radiative transfer models of the pumping of CO_2. Models neglecting the effect of dust produce strong emission in the 15 μm region; when dust is taken into account, absorption results. However, these models cannot reproduce the spectra of those O-rich AGB stars that show emission at 13.87 and 16.18 μm and absorption at 14.98 μm. Furthermore, these models predict absorption at 4.3 μm which is not observed.

The chemical pathway for the formation of CO_2 in the extended atmosphere is recently explained by Duari et al. (1999). While thermal equilibrium calculations yield a rather low CO_2 abundance, shock chemistry provides the solution to form CO_2 in large amounts. At small radii the dominant pathway for the formation of CO_2 is

$$\mathrm{OH} + \mathrm{CO} \rightarrow \mathrm{CO_2} + \mathrm{H} \quad (1)$$

where the OH is formed from the collisional destruction of water. At larger radii ($R > 2R_*$) the dominant pathway is

$$\mathrm{CO} + \mathrm{O} + \mathrm{M} \rightarrow \mathrm{CO_2} + \mathrm{M} \quad (2)$$

producing a significant increase in CO_2 abundance (up to 6 10^{-5}) although the reaction rate is quite uncertain.

In this paper we present a detailed analysis of the CO_2 bands as observed by ISO/SWS in EP Aqr. The CO_2 emission bands are most pronounced in the spectrum of this object; the excellent quality of the data - high resolution and high S/N - makes this object an ideal testcase for comparing data with models. We performed LTE model calculations including optical depth effects for a simple geometry with one CO_2 layer in order to produce synthetic spectra that can be directly compared to the ISO/SWS observations.

Sect. 2 summarizes the most important background information on EP Aqr. In Sect. 3 we present the data and the necessary data reduction processes used to obtain a high resolution and high S/N spectrum. Sect. 4 describes in detail how our model is constructed, how the different parameters change the appearance of the output spectra and how a quantitative comparison is made between models and observations. Sect. 5 discusses the results of this comparison. These results are discussed in the framework of hydrodynamical model atmospheres, pulsations and dust formation in Sect. 6.

2. EP Aqr

EP Aqr is an M8 star classified as an SRb variable with a period of 55 days (although this period is uncertain), at a distance of 135 parsec Knapp et al. 1998, Perryman et al. 1997. The light curve shows a variable amplitude.

Knapp et al. 1(1998) obtained high velocity resolution profiles of the CO(2-1) and CO(3-2) lines in this object, clearly revealing the presence of two components in the outflow, both centered at a radial velocity of -33 km/s. The first (broad) component has an outflow velocity of 10.8 $\pm$ 1.0 km/s while the second (narrow) component has a velocity width of only 1.5 $\pm$ 0.3 km/s. The mass loss rates derived from these observations are 2.3 10^{-7} and 1.7 10^{-8} respectively. The authors suggest that the narrow component may be due to the resumption of mass loss after it has been stopped by some change in the stellar properties. However, as the line profile of the narrow component has a gaussian rather than a parabolic profile, it is also possible that this star has a wide circumstellar disk; similar observations are analyzed by Jura & Kahane (1999).

Both the IRAS LRS and ISO/SWS spectra of EP Aqr clearly show silicate dust emission at 10 and 18 μm and a dust feature at 13 μm. Justtanont et al. (1998) showed that there is a correlation between the strength of the 13 μm dust feature in the spectra of O-rich AGB stars and the strength of the CO_2 bands. The equivalent width of the 13 μm feature is the largest in EP Aqr. Many possible carriers for this feature have been proposed, but $MgAl_2O_4$ (spinel) seems to be the most convincing candidate Posch et al. 1999. The correlation of the strength of the 13 μm feature with the presence of CO_2 suggests that the formation of both species is favoured by the same physical conditions.

3. ISO observations and data reduction

The data discussed in this paper is the SWS full resolution scan (AOT06) of EP Aqr in the wavelength range 12-16.5 μm (AOT band 3a) observed on 4 May 1997. The data were reduced with the SWS Interactive Analysis (IA) data reduction software package using standard ISO pipeline products (version 7.0) at the ISO datacenter in Groningen. The observed wavelength range is scanned twice in different directions (the up- and down-scan). Variations in dark currents and memory effects in the detectors generally produce differences in the fluxes seen in the up and down scan. In this AOT band however, memory effects are small and dark currents are negligible compared to the high fluxes.

From overlaying the up- and down-scan for each of the 12 detectors in this AOT band, it is found that differences between the up- and down-scan due to cosmic-ray glitches or signal jumps are very scarce and only present at the 2 % level. The main uncertainties in this wavelength range arise from instrumental fringing. In principle a plain division of the data with the Relative Spectral Response Function (RSRF) should correct for this, but this is not the case as the RSRF is determined from pre-flight measurements on extended calibration sources. As a consequence, the fringe pattern is not sampled at the resolution obtained for point sources, resulting in fringe amplitude differences between data and RSRF. Moreover, pointing offsets cause the observed fringe pattern to be slightly shifted with respect to the RSRF. Although there exist several tools in IA to 'defringe' the spectrum after the responsivity calibration, we found that for this kind of high-resolution observations these tools are confused by the overwhelming amount of (relatively regular) strong CO_2 emission lines in the spectrum. None of the present defringing tools is able to get rid of the fringes without also changing the CO_2 spectrum. Therefore we chose another strategy and performed the responsivity correction interactively using the `resp_inter` routine. First, data and RSRF were divided in a high number (15-20) of bins of the same width. For each of the bins that do not contain strong CO_2 emission bands, the RSRF was shifted in wavelength direction until the fringes in the RSRF were coincident with those in the data. The shifts thus found are virtually the same for all bins. Next, we enhanced the RSRF in each of these bins in order to minimize the residuals after division. The enhancement factors show a slight decrease with increasing wavelength, as is expected when the resolution increases with increasing wavelength. The shifts and enhancement factors for the bins that do show strong emission bands are an interpolation between the values found for the adjacent bins. This procedure removes most of the fringes - although residuals are still present in some parts of the spectrum, especially in the 12 - 13 μm region where the RSRF drops below 30 % of the peak value. The observed emission lines however are present in both the up and the down-scan at the same flux level and not in the RSRF, confirming that the observed lines are real (see Fig. 1). The main uncertainties left are possibly broad features that influence the underlying continuum. Next, the absolute flux levels of the different detectors are aligned and finally the spectrum is rebinned. Narrow lines that are clearly present in both the up- and down-scan (see Fig. 1) allowed us to determine the actual resolution for this particular observation from the measured FWHM of these lines. We found a typical resolution of about 2800 at 15.3 μm, 40 % higher than generally assumed. We finally rebinned the spectrum with a constant resolution of 2500 specifying an oversampling rate of 1 and applied a radial velocity correction to the whole spectrum. The resulting spectrum is shown in Fig. 2.

The IA package provides an estimate of the uncertainties on the datapoints in the rebinned spectrum which are determined by calculating the variance of the flux values of the different detectors for each bin. However, when reducing both the up- and down-scan separately, it is found that the differences between these scans are often larger than these uncertainties. For those points where this is the case, we adopted the difference between up- and down-scan as the observational uncertainty.

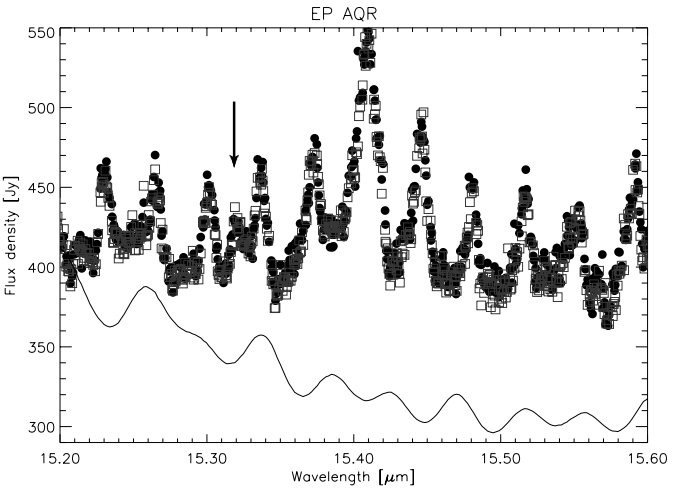

Fig. 1. A representative part of the spectrum of EP Aqr before rebinning. Closed circles are the data for all detectors in the down-scan, open squares are for the up-scan and the solid line is the RSRF for one of the detectors, scaled and shifted for the sake of clarity. The nearly perfect match between both scans illustrates the excellent quality of the data. All lines are present in both scans, and not in the RSRF, confirming that the fringes have been well removed and the lines are real. Note also the clear presence of a CO_2 line at 15.32 μm (indicated by the arrow), suggesting that the SWS resolution is higher than previously thought.

4. Modeling the emission lines

4.1. Line data

In the observed spectrum (see Fig. 2) obvious strong emission bands are present at 13.48, 13.87, 14.98, 15.40 and 16.18 μm. Justtanont et al. (1998) identified these strong bands with rovibrational Q-branch bands of $^{12}CO_2$ and $^{13}CO_2$. Furthermore there is a forest of (weaker) P- and R- lines clearly visible over almost the entire observed wavelength range. The main spectral difference between $^{12}CO_2$ and $^{13}CO_2$ is the shift of the fundamental bending mode from 14.98 μm for $^{12}CO_2$ to 15.40 μm for $^{13}CO_2$. The presence of the fundamental bending mode of $^{13}CO_2$ is necessary to reproduce the peak intensity at 15.40 μm(see Fig. 4). The other Q-branch bands do not show such clear evidence for the presence of $^{13}CO_2$ but may show up as a shoulder in the wing of the corresponding $^{12}CO_2$ band (e.g. around 16.2 μm).

We searched the HITRAN database (Rothman et al. 1987, 1992) for all known transitions of both $^{12}CO_2$ and $^{13}CO_2$ that fall in the observed wavelength range. Fig. 3 shows the vibrational level scheme of $^{12}CO_2$ and $^{13}CO_2$ and the main infrared active vibrational transitions involved. There are 3 normal modes : 2 stretching and 1 bending mode. The ν_1 symmetric stretching mode is a $\Sigma_g^+ - \Sigma_g^+$ type transition and hence is infrared inactive. The ν_2 bending fundamental band (at 14.98 μm)

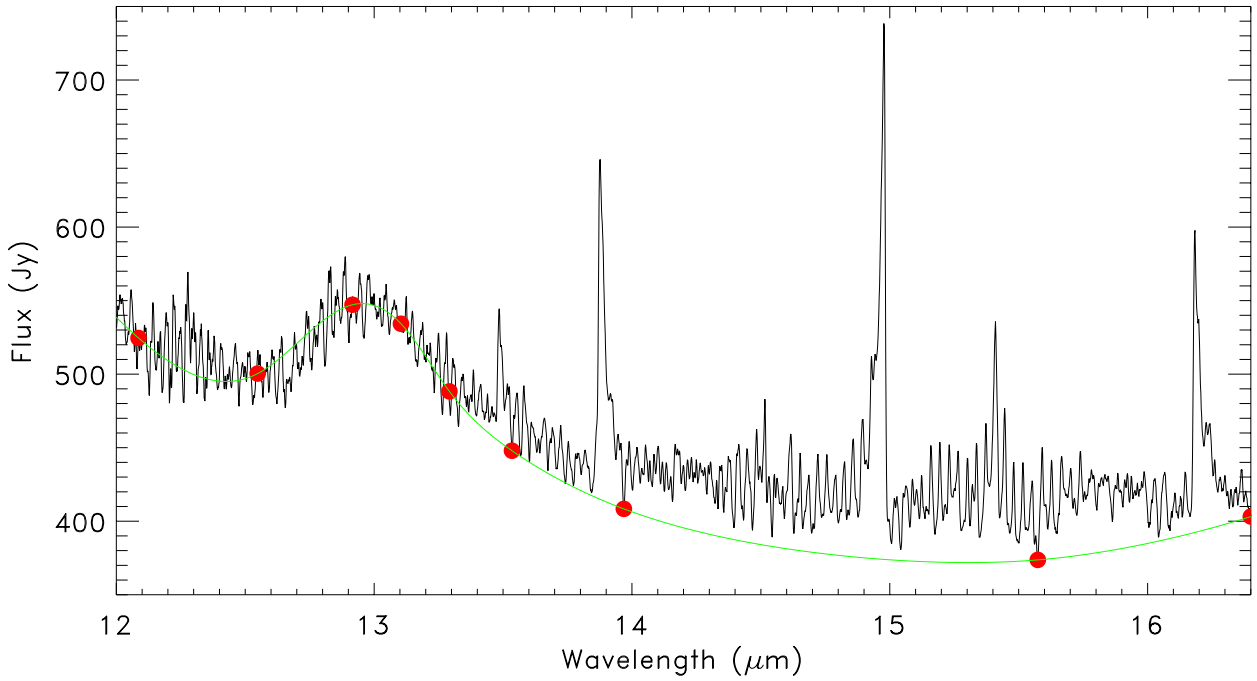

Fig. 2. The full AOT band 3a spectrum of EP Aqr after rebinning. Between 12 and 13 μm the RSRF drops to very low values and moreover there are no obvious CO_2 bands in this wavelength range. We therefore consider the rapid variations in this part to be mainly due to fringe resiudals superposed on the continuum. The solid circles define the continuum used for the analysis of the CO_2 bands. Assuming that the 13 μm feature is the only dust feature in this wavelength region, we chose only a few points longward of 13 μm in order to obtain a smooth continuum. The grey line is a spline fit through these points and is used as a continuum when comparing data and models.

is a perpendicular transition; this band has a strong Q branch band. More perpendicular transitions arise from the degenerate excited states, having subsequently slightly higher frequencies than the fundamental (see Fig. 3). The intrinsically strongest band is the ν_3 antisymmetric stretching fundamental band at 4.25 μm. This is a $\Sigma_u^+ - \Sigma+_g$ type transition and hence only exhibits P and R branches. Furthermore there are combination bands, e.g. at 13.48 and 13.87 μm.

From the transition probabilities R_{lu} given in HITRAN we can calculate the Einstein A coefficient for each transition as Rybicki & Lightman (1979)

$$A_{ul} = \frac{g_l}{g_u} \frac{64\pi^4 \nu_{ul}^3}{3hc^3} R_{lu} \quad (3)$$

where g_l and g_u are the statistical weigths respectively for the lower and upper level considered and ν_{ul} the frequency of the transition.

4.2. The model

We modeled the observed emission lines using a single layer, plane-parallel LTE model with a stellar background.

4.2.1. The background continuum

The stellar continuum is approximated by a blackbody with a given effective radius R_* and effective temperature T_*. Engelke (1992) derived an analytical expression to correct for H^- free-free opacity in this wavelength range. We used this expression to determine R_* and T_* from the observed continuum in the short wavelength part of the SWS AOT1 low-resolution scan with complete wavelength coverage (2 - 45 μm). This observation was performed right after the AOT6 observation as part of the STARTYP program (PI S. Price). We derived R_* = 264 $R_\odot$ and T_* = 2447 K for a distance of 135 parsec and used these values as input for the corrected blackbody stellar background.

The main contribution to the continuum in the 15 μm region however comes from circumstellar dust. The SWS spectra show the silicate bands in emission and a strong 13 μm dust feature. Assuming that the dust emission is optically thin and that it is located further out than the CO_2 emitting layer, the dust continuum is merely an additive term in the final spectrum and we can hence neglect this term by comparing the continuum subtracted model- and observed spectrum. We determined the continuum in the observed spectrum by fitting a cubic spline through the 13 μm feature and determining the onset of the 18 μm silicate band (see Fig. 2). This determination is rather ad hoc and may significantly influence the results. A discussion of this point is given in Sect. 4.4.

4.2.2. The CO_2 layer

In front of the star we put a single circular slab of molecules for which the temperature T, the column density N and the radius $R_{\rm em}$ is specified. This radius $R_{\rm em}$ is larger than R_*, causing the inner part of the slab to absorb the stellar radiation, while

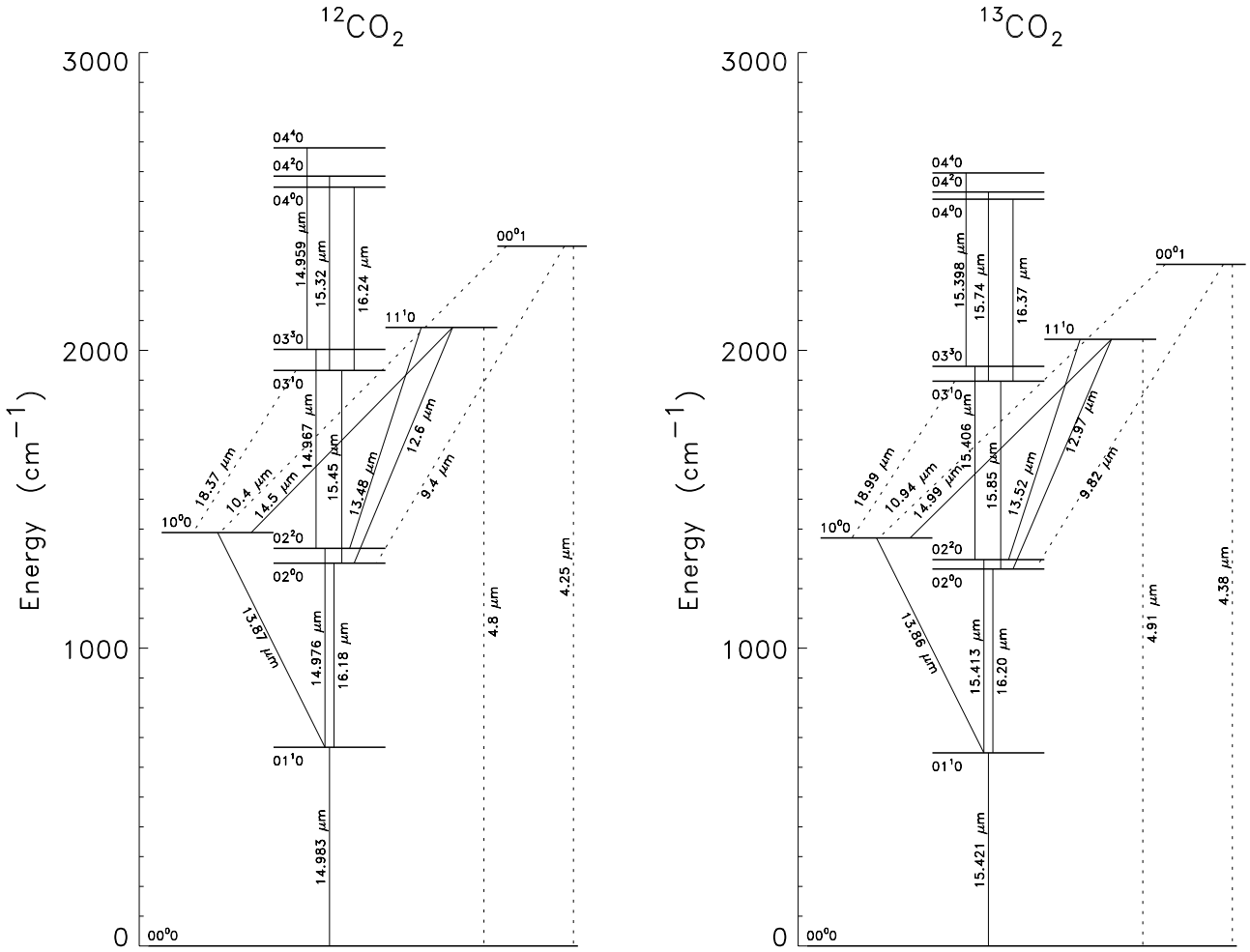

Fig. 3. Energy diagram for $^{12}CO_2$ and $^{13}CO_2$. The vibrational levels are labeled using the notation of Herzberg (1945). Solid lines indicate transitions that fall in the observed wavelength range; dashed lines are transitions that fall outside the observed wavelength range. Note that not all of the bands show a Q-branch band (e.g. at 9.4 and 10.4 μm). The main difference between $^{12}CO_2$ and $^{13}CO_2$ is that the fundamental bending mode is shifted from 14.98 to 15.4 μm.

the whole layer produces emission. This is basically the same model as used by Yamamura et al. (1999a; 1999b).

Assuming the lines to be formed in LTE, the population distribution over the levels (both rotational and vibrational) only depends on T and can be calculated using the Boltzmann equation

$$\frac{N_u}{N} = \frac{g_u}{\mathcal{Q}(T)} e^{-(E_u/kT)} \tag{4}$$

with g_u the statistical weight of the upper level, E_u the energy of the upper level with respect to the ground state energy and where

$$\mathcal{Q}(T) = \sum_i g_i e^{-(E_i/kT)} \tag{5}$$

is the partition function at temperature T, summing over all possible energy states. These parameters are all supplied by the HITRAN database.

Next we calculate the optical depth assuming that turbulent motions in the gas are the main source for line broadening. As the Einstein A coefficients are rather small, natural broadening will be negligible and hence we can use a Gaussian line profile. The optical depth is calculated on a high frequency resolution grid in order to accurately sample the optical depth profile. Taking stimulated emission into account, the optical depth τ_ν at a frequency ν for a transition at rest frequency ν_0 is given by

$$\tau_\nu = \frac{h\nu_0}{4\pi}\phi(\nu,\nu_0)(N_l B_{lu} - N_u B_{ul}) \tag{6}$$

with B_{lu} and B_{ul} the Einstein coefficient for absorption and stimulated emission respectively and where the normalized gaussian line profile function $\phi(\nu,\nu_0)$ is

$$\phi(\nu,\nu_0) = \frac{1}{\Delta\nu_D\sqrt{\pi}} e^{-(\nu-\nu_0)^2/(\Delta\nu_D)^2} \tag{7}$$

with $\Delta\nu_D = \nu_0 \frac{v_{\rm turb}}{c}$ the Doppler width. Using the Einstein relations

$$g_l B_{lu} = g_u B_{ul} \tag{8}$$

$$A_{ul} = \frac{2h\nu^3}{c^2} B_{ul} \tag{9}$$

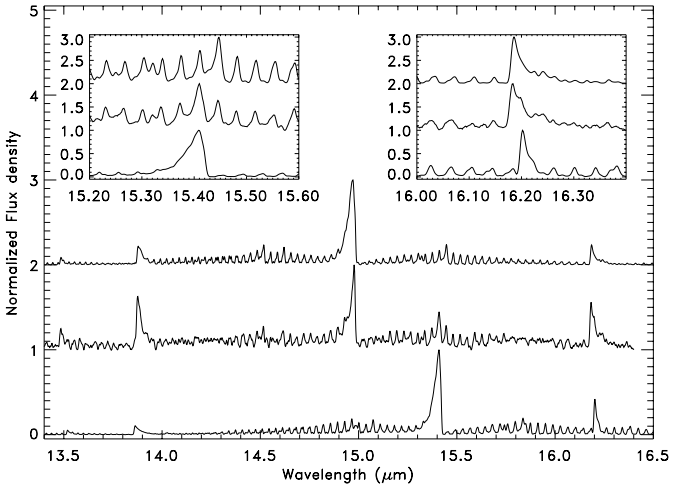

Fig. 4. The spectral difference between $^{12}CO_2$ and $^{13}CO_2$. Top : pure $^{12}CO_2$ T=800 K, N=10^{18} cm^{-2}; Bottom : pure $^{13}CO_2$ T=800 K, N=10^{18} cm^{-2}; middle : the observed continuum subtracted spectrum of EP Aqr. All spectra are normalized to the maximum intensity and are hence only illustrative for the different band positions, not the band intensities. The insets show blow-ups of the 15.4 and 16.2 regions.

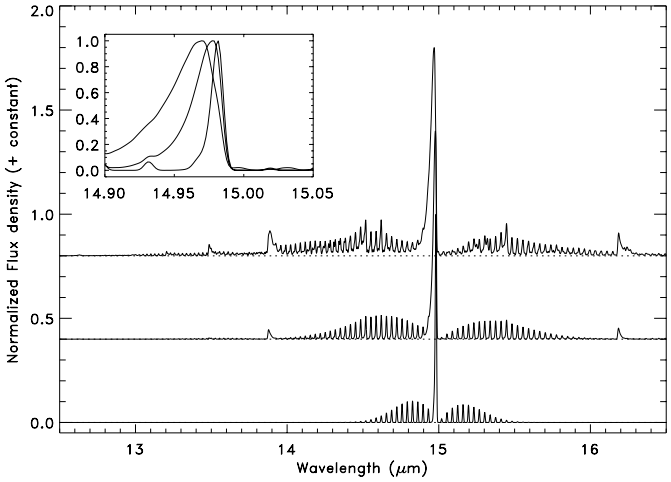

Fig. 5. The effect of changing the temperature T of the CO_2 layer (for optically thin models). The lower spectrum is a model with T=100 K, the middle T=400 K and the top one with T=800 K. The inset shows a blow-up of the 15 μm region for the three models. All models are normalized to the peak flux.

and the Boltzmann equation

$$\frac{N_l}{N_u} = \frac{g_l}{g_u} e^{(h\nu/kT)} \tag{10}$$

we can rewrite Eq. (6) as

$$\tau_\nu = \frac{N_u A_{ul} h\nu_0}{4\pi B_\nu(T)} \phi(\nu, \nu_0) \tag{11}$$

The final profile is the sum of the profiles of all transitions considered. We used a turbulent velocity $v_{\rm turb}$ of 3 km/s; this is a typical value for the acceleration region Höfner & Dorfi 1997. If a molecular layer is desired with more than one chemical component, optical depths are calculated for each component separately and summed. In this particular case we want to include both $^{12}CO_2$ and $^{13}CO_2$ in the model if necessary (see Fig. 4).

The formal solution of the radiative transfer equation is given by

$$I_\nu(\tau_\nu) = I_\nu^0 e^{-\tau} + \int_0^{\tau_\nu} e^{-(\tau_\nu - \tau'_\nu)} S_\nu(\tau'_\nu) d\tau'_\nu \tag{12}$$

where I_ν^0 denotes the background intensity and S_ν the source function. In LTE, $S_\nu = B_\nu(T)$ and in our single layer model this is constant. Hence the solution of the radiative transfer equation becomes

$$I_\nu(\tau_\nu) = I_\nu^0 e^{-\tau_\nu} + B_\nu(T)(1 - e^{-\tau_\nu}) \tag{13}$$

and with $I_\nu^0 = 0$ for $R_{\rm em} > R_*$ the total emitted flux can be calculated by

$$F_\nu = \pi(\frac{R_*}{D})^2 [I_\nu^0 e^{-\tau_\nu} + (\frac{R_{\rm em}}{R_*})^2 B_\nu(T)(1 - e^{-\tau_\nu})] \tag{14}$$

with D the distance to the star. Finally, the spectrum is convolved with the instrumental profile which is assumed to be a Gaussian with a FWHM determined by the resolution and rebinned to the SWS resolution.

4.3. The parameters and their influence

The model as described above has essentially 3 free parameters for a given chemical composition : T, N and $R_{\rm em}$. Changing any of the parameters can considerably change the output spectrum.

4.3.1. The temperature T

The temperature T of the CO_2 layer is the most important parameter in the model. Changing the temperature redistributes the molecules over the different energy levels and this has several consequences for the resulting output spectrum, as illustrated in Fig. 5.

At low temperatures, most of the molecules are in the ground state. Only a very small fraction of the molecules can get excited to even the lowest vibrational level, and hence only the fundamental bending mode at 14.98 μm is present in the spectrum. Increasing the temperature of the CO_2 layer causes a redistribution of the CO_2 molecules in which the higher vibrational energy levels become more populated. The most obvious effect on the resulting spectrum is the appearance of bands arising from these higher levels, as can be seen from Figs. 3 and 5. A secondary effect of this vibrational redistribution is the contribution of hot bands to the spectrum. As the hot bands of the fundamental bending mode (at 14.98 μm) have wavelengths consecutively to the blue, higher temperatures cause the peak of the band around 15 μm to shift to the blue (see Fig. 5).

Also the higher rotational levels within a given vibrational level will become more populated at higher temperatures. The Q-branches will consequently become broader (see the inset in Fig. 5), which is also true for the P- and R- branches; furthermore

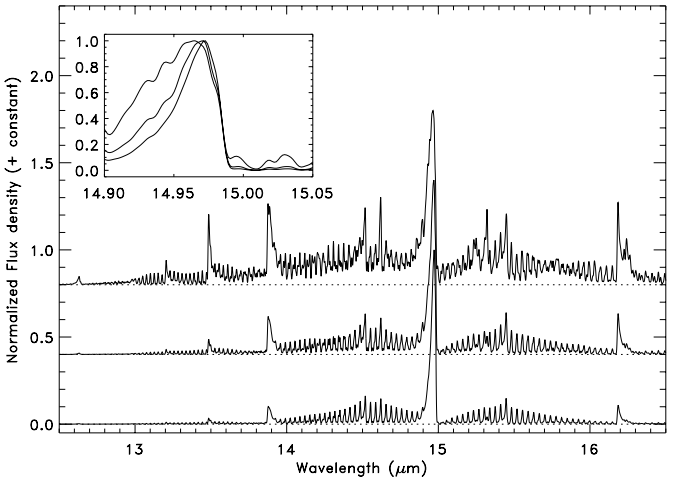

Fig. 6. The effect of changing the column density N of the CO_2 layer. All models have T=600 K. The lower is a model with N=10^{17} cm^{-2}, the middle N=10^{18} cm^{-2} and the top one N=10^{19} cm^{-2}. The inset shows a blow-up of the 15 μm region for the three models. All models are scaled to the peak flux.

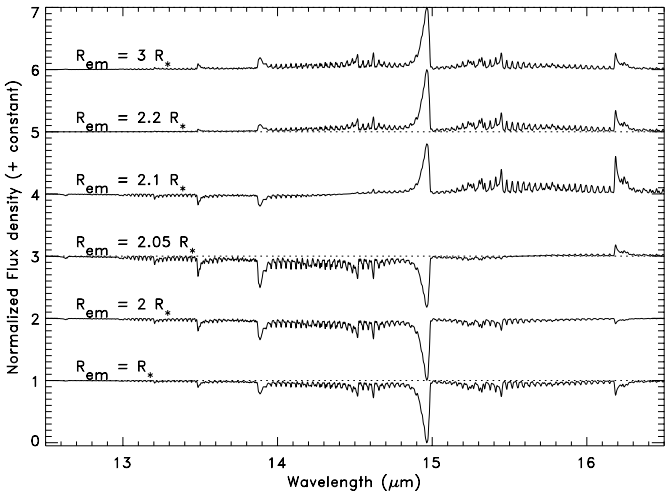

Fig. 7. The effect of changing the radius of the emitting region. All models have T=800 K and N=10^{18} cm^{-2}. From top to bottom, $R_{\rm em}$=3 R_*, $R_{\rm em}$=2.2 R_*, $R_{\rm emi}$=2.1 R_*, $R_{\rm em}$=2.05 R_*, $R_{\rm em}$=2 R_*, $R_{\rm em}$= R_*; for the sake of clarity, the output spectra are first divided by the continuum and subsequently scaled to show the same contrast.

the peak of these P- and R- bands will move away from the Q-branch.

A final remark concerns the global intensity of the output spectrum. Although the optical depth in the lines generally decreases with increasing temperatures (as higher vibrational levels become more populated), the output intensity is generally higher for models with a higher temperature. This is mainly because the source function increases with increasing temperature, but also because more transitions become excited.

4.3.2. The column density N

Changing the column density N can also severely affect the output spectrum (see Fig. 6). Increasing the column density will increase the optical depth at any given wavelength. As long as all lines are optically thin, this will only scale the entire output spectrum to higher fluxes.

The first lines to become optically thick are the Q-branch lines around 15 μm. Increasing the column density will then start deforming the output spectrum as weaker lines gain more in intensity than the optically thick lines. This results in three types of changes, often similar in appearance to increasing the temperature T.

First of all, the Q-branch band itself becomes broader. When the cores of the lines that contribute to the band are optically thick, their wings will start producing a significant contribution to the output flux. Moreover, the higher energy transitions also gain in relative importance to the output flux. As can be seen from Fig. 6, the peak position of the 15 μm band shifts slightly to the blue, as also the hot bands start contributing to the output spectrum.

A second effect is that the relative intensities of the P- and R- branches increase slightly with respect to the Q-branch, due to the same effect. And finally, whole regions of the spectrum can become optically thick and thus produce a "continuum"-like deformation in the spectrum. This is especially the case in the regions next to the 15 μm band, where there is a dense forest of lines arising from different vibrational levels; when the column density is sufficiently high, they all contribute significantly to the spectrum, also in their wings, and this produces the deformation. In the limit of infinite column densities, $\tau_\nu \rightarrow \infty$ for all frequencies and the output spectrum is a Planck function at temperature T as can be easily seen from Eq. (14).

4.3.3. The size of the emitting region, $R_{\rm em}$

The size $R_{\rm em}$ of the circular CO_2 slab determines in the first place whether the spectrum shows absorption lines or emission lines. If the slab has the same size as the star, a pure absorption spectrum results (see Fig. 7) unless $T \geq T_*$. Enlarging $R_{\rm em}$ will cause the part that geometrically extends beyond the star to produce emission that gradually fills up the absorption lines, and eventually results in net emission. This happens first at longer wavelengths where the background continuum has a lower intensity and hence the absorption is weaker; in such cases the result is a spectrum where the red part can be seen in emission while the blue part is still in absorption. The turnover to a net emission spectrum happens in a very small range of $R_{\rm em}$. When $R_{\rm em}$ is much larger than this critical radius, the output spectrum is dominated by the emission and increasing the radius will then just scale up the output spectrum.

In summary we conclude that :

- the temperature T will cause the 14.98 μm band to broaden and shift to the blue; high temperatures are required to explain the presence of hot bands in the spectrum.
- the column density N determines the relative band intensities and bandwidths.

– the extent R of the emitting region determines the peak intensities.

Although this is a rather simple model, it reproduces quite well the observed band profiles (see Figs. 10 to 14). The next section describes how these fits are obtained.

4.4. Determining the model parameters

4.4.1. Quantifying the quality of the fit

In order to derive the model parameters that provide the best fit to the observations, a quantitative comparison between the model spectrum and the observed spectrum needs to be made. This is done by calculating

$$\chi^2_\nu = \frac{\chi^2}{\nu} = \frac{1}{N_\mathrm{p} - m} \sum_i \frac{(y_o - y_m)^2}{\sigma^2} \quad (15)$$

where y_o and y_m are the continuum subtracted flux values for the observations and the model respectively; σ are the uncertainties on the data points (assuming that the uncertainties on the model spectrum are negligible); the sum runs over all data points N_p in the wavelength range considered and $\nu = N_\mathrm{p} - m$ is the number of degrees of freedom with m the number of free parameters.

For a good fit, χ^2_ν should be low, of order unity. If χ^2_ν is much larger however, this does not necessarily mean that the adopted model is a bad fit to the observations; a large χ^2_ν value can indicate a doubtful error assignment or the presence of *systematic* errors in the data.

We first minimized χ^2_ν using a model with only 3 free parameters, T, N and R. It turns out that the best fit in this case yields unreasonably high optical depths while the χ^2_ν remains quite large. A systematic error in the determination of the continuum in the observations causes the line contrast to change in such a way that high optical depths are required to reproduce the line shape and the relative intensities; this is related to the broadband deformation for high column densities as described in Sect. 4.3. We therefore allowed the continuum to shift up and down in intensity (while keeping the shape as determined from Fig. 2) and introduced this shift as an extra free parameter in the model and minimized the χ^2_ν again. The new χ^2_ν values are much lower while the derived continuum shift is small compared to the line intensities. In order to assess the significance of this parameter, we used the F-test of an additional term on this parameter (Bevington & Robinson 1992, chapter 11). We calculated

$$F_\chi = \frac{\Delta\chi^2}{\chi^2_\nu} \quad (16)$$

where $\Delta\chi^2$ is the change in χ^2 when comparing the best fit with and without adding the extra parameter and χ^2_ν corresponds to the best fit value with the extra parameter added. This ratio is a measure of how much the additional term has improved the value of the reduced chi-square and should be small when the function with the added parameter does not significantly improve the fit over the function without the added term. Using the associated F distribution function, one can evaluate the probability of obtaining the observed value of F_χ when the added parameter would be superfluous. In our case, the probabilities are lower than 10^{-3} for all bands, indicating that introducing the continuum shift as an extra parameter is justified. Therefore we included this continuum shift for the entire minimization procedure. Allowing also for a change in the slope of the continuum on the other hand did not significantly improve the χ^2_ν.

4.4.2. Searching parameter space

The model parameters that provide the best fit to the observations are those for which $\chi^2_\nu(T, N, R_\mathrm{em})$ has a minimum. We defined a grid in T between 100 K and 900 K in steps of 50 K, and a logarithmically equidistant grid in N in the range 10^{16} cm^{-2} - 10^{25} cm^{-2}. At each of the grid points radiative transfer is calculated for the given T and N and with the `amoeba` downhill simplex method (Press et al. 1992, Sect. 10.4) we determined at the same time the value of R_em and the continuum shift that minimizes the χ^2_ν to a fractional tolerance of 10^{-10}.

As the observed spectrum of EP Aqr shows Q-branch bands arising from vibrational levels at a very different energy, it is likely that these bands are formed at different locations and hence different excitation temperatures. Instead of fitting the whole spectrum we therefore determined the parameters for each of the bands individually by defining a spectral window of 0.4 μm around the bands, centered at the band head. This includes the whole Q branch and typically 10-15 P and R branch transitions per vibrational transition.

After the first run we introduced the ^{12}C/^{13}C ratio as another free parameter and calculated the corresponding F_χ values. This significantly improves the χ^2_ν for all bands except for the 13.48 μm band which is apparently less sensitive to the contribution of $^{13}CO_2$. We therefore also defined a grid in ^{12}C/^{13}C ratio values of 1, 5, 10, 15, 20, 25, 30, 40, 50, 60, 70, 100; these values were chosen to adequately sample the range of values typically found in AGB stars Dominy & Wallerstein 1987; Smith & Lambert 1985, 1986; Sneden et al. 1986.

4.4.3. The model parameters and their uncertainties

Once the χ^2_ν is calculated on the grid points, the values of the ^{12}C/^{13}C ratio, T and N and the uncertainties on these parameters can be derived in the following way (Bevington & Robinson 1992, Sect. 11.5). Fig. 8 shows a two-dimensional projection of the χ^2_ν hypersurface onto the (^{12}C/^{13}C ratio, T) plane. For each (^{12}C/^{13}C ratio, T) grid point, there are 19 χ^2_ν values that were calculated for each of the grid points in N. For this projection, we only consider the minimum of these 19 values. The values for the ^{12}C/^{13}C ratio and T that provide the best fit to the data thus correspond to the minimum χ^2_ν in this projection. A 1 σ contour on the derived parameters in this projection is then found by evaluating for which (^{12}C/^{13}C ratio, T) values $\chi^2 < (\chi^2_\mathrm{min} + 1)$. Projecting the outer edges of this contour onto the ^{12}C/^{13}C ratio axis gives the 1 σ uncertainties on the derived ^{12}C/^{13}C ratio; projection on the T axis yields

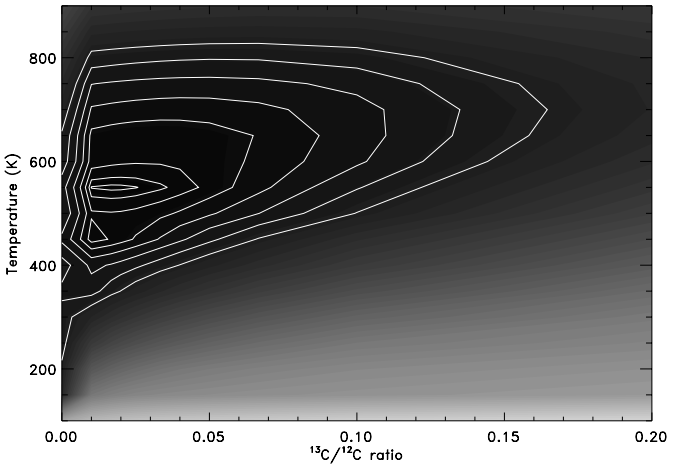

Fig. 8. Two-dimensional projection of the χ^2_ν contours in the $(^{13}\mathrm{C}/^{12}\mathrm{C}, T)$ plane for the 16.18 μm band. The contours enclosing the minimum are 1σ, 2σ, ..., 10σ contours.

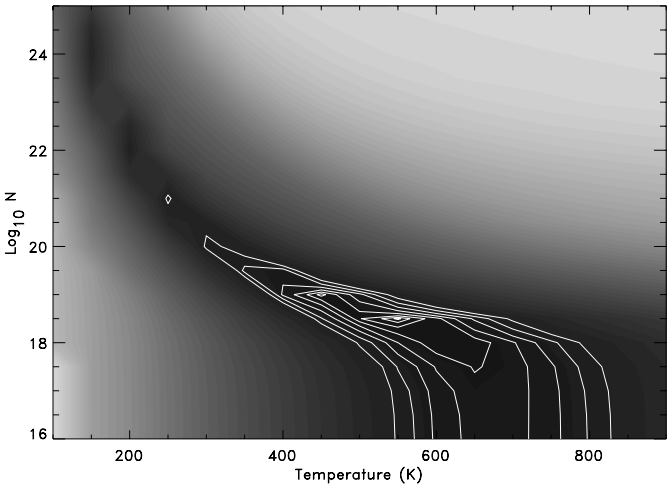

Fig. 9. Same as Fig. 8 but for the (T,N) plane.

Table 1. The derived parameters for all the bands using a single layer LTE model. The errors stated are the formal errors based on the χ^2_ν analysis.

λ_c (μm)	T (K)	$\log N$ (cm^{-2})	R (R_*)	$^{12}\mathrm{C}/^{13}\mathrm{C}$	$\tau_{\max}$
13.48	700^{+25}_{-25}	$18.5^{+.25}_{-.25}$	$4.4^{+1.0}_{-0.5}$	-	$1.5^{+1.2}_{-0.7}$
13.87	500^{+25}_{-25}	$18.5^{+.25}_{-.25}$	$8.6^{+1.3}_{-1.0}$	$10^{+2.5}_{-2.5}$	$3.8^{+2.9}_{-2.9}$
14.98	350^{+25}_{-25}	$19.0^{+.25}_{-.25}$	$9.0^{+0.3}_{-0.4}$	$100^{+?}_{-20}$	225^{+176}_{-99}
15.40	450^{+25}_{-25}	$18.5^{+.25}_{-.25}$	$7.2^{+1.0}_{-0.7}$	$30^{+2.5}_{-2.5}$	$21.9^{+17.1}_{-9.6}$
16.18	550^{+25}_{-25}	$18.5^{+.25}_{-.25}$	$7.2^{+1.3}_{-0.8}$	60^{+40}_{-20}	$3.2^{+2.5}_{-1.4}$

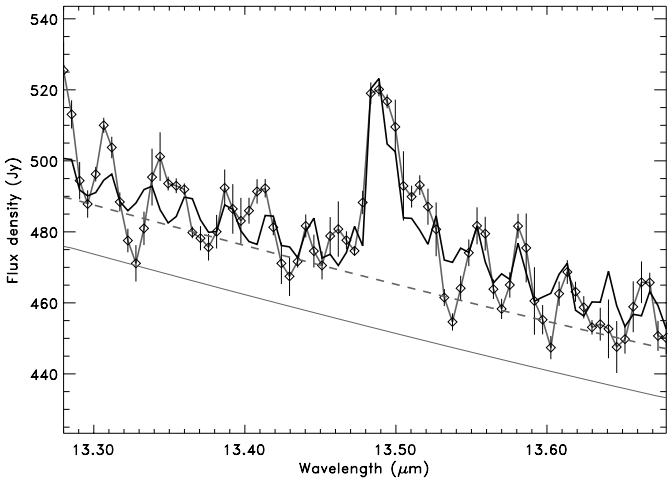

Fig. 10. The 13.48 μm region. The SWS observations are the diamonds connected with the grey line; the observational uncertainties are indicated by the vertical lines. The solid line is the best fitting model (see Table 1). The dotted line is the continuum as in Fig. 2; the dashed line indicates the continuum shift derived by the minimization procedure. Note the fringe residuals in this wavelength region.

the uncertainties on the temperature. In a similar way one can also determine the uncertainties on N by making a projection onto the (T, N) plane (see Fig. 9). However, as we only have the χ^2_ν values for the predefined grid points, the accuracy is at best limited to the grid spacing.

For R and τ we have no predefined grid and so the uncertainties on these parameters have to be estimated in another way. Both parameters depend on T and N; around the minimum however, they are affected mainly by N as the grid spacing is logarithmic for this parameter. We therefore changed N to within the derived 1 σ uncertainties while keeping the T at its best value and then determined the R that minimizes the χ^2_ν; the resulting R values corresponding to the extreme N values were subsequently taken as the uncertainties on R. As $\tau \propto N$ it is straightforward to calculate the change in τ when changing N and also here we took the extremes as uncertainties on τ. We note however that the χ^2 corresponding to these extremes deviates by more than one from the minimum χ^2 value; therefore these formal uncertainties are probably rather conservative.

5. Results

Table 1 lists the derived parameters and their uncertainties obtained from the χ^2_ν for the different bands. The corresponding best fits can be seen in Figs. 10 to 14. For *all* the bands the derived parameters yield a maximum optical depth $\tau_{\max} > 1$ for each of the spectral windows. As the optically thin models are a subset of the parameter space we studied, the first obvious conclusion is that the observations are better explained by an optically thick model than an optically thin one.

It can easily be seen from Eq. (14) that for the case of optically thick bands $F_\nu \propto B_\nu R^2_{\mathrm{em}}$ and hence in our model the observed peak intensity is a good measure of the extent R of the emitting region.

5.1. Temperatures

The whole spectrum cannot be reproduced at once by a single layer model. The temperatures derived for the individual bands are significantly different, reminiscent of a temperature strat-

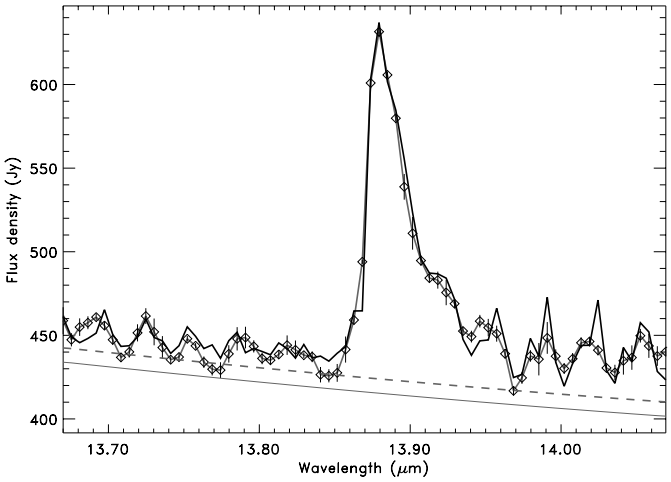

Fig. 11. Same as Fig. 10 for the 13.87 μm region.

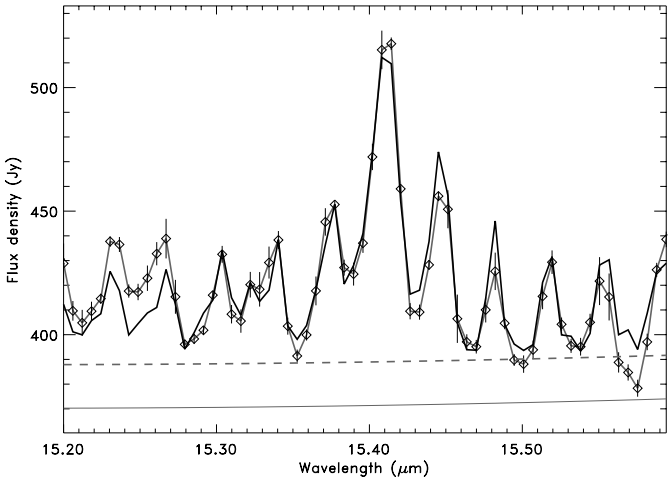

Fig. 13. Same as Fig. 10 for the 15.40 μm region.

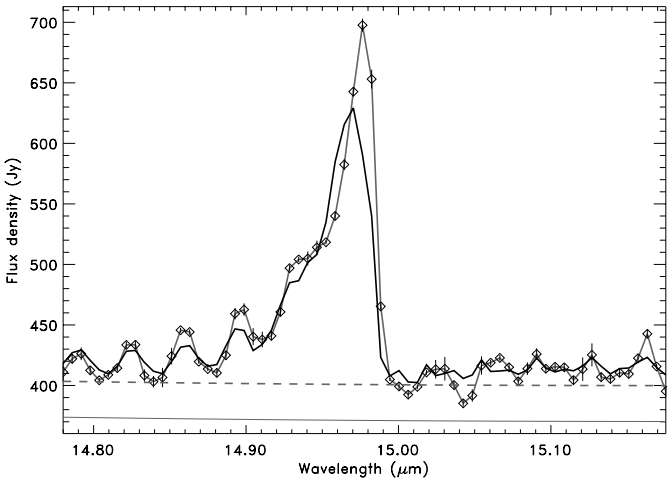

Fig. 12. Same as Fig. 10 for the 14.98 μm region. Note the sharp peak indicating the presence of a much cooler layer on top of a warmer layer.

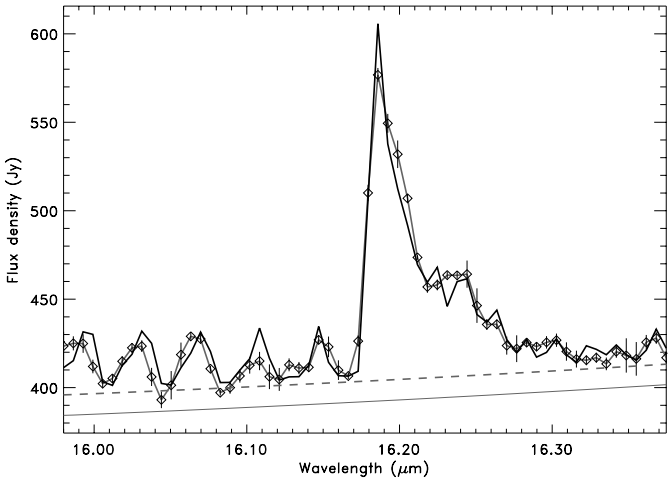

Fig. 14. Same as Fig. 10 for the 15.40 μm region.

ification in the extended atmosphere. Q-branch bands arising from higher vibrational levels are then probing the hotter material closer to the central star, while the emission from lower vibrational levels arises from cooler material further out.

However, as can be seen from Fig. 5, any given band becomes stronger when increasing the temperature. When deriving the parameters for a given band, one might therefore expect to see a significant contribution from the hotter layers as those hotter layers always show stronger emission in the bands arising from lower vibrational levels (see Fig. 5). However, as a consequence of all the bands being optically thick, emission from the hotter layers is shielded from view at those wavelengths where a cooler layer shows prominent emission features. On the other hand, a contribution from the cooler layers might be present at those wavelengths in the spectrum where the hotter layers are visible if the cooler material is optically thin at those wavelengths.

As a consistency check we therefore performed a test calculation for the 13.48 and 13.87 μm bands with a two-layer model using the parameters from Table 1. The 13.87 μm band is indeed quite unaffected by the presence of the $T = 700$ K layer, but the flux in the 13.48 μm band shows a significant contribution due to the $T = 500$ K layer. The main effect is that the extent $R_{\rm em}$ for the warmer layer decreases when compared to the single layer model and thus the $R_{\rm em}$ values listed in Table 1 are probably too high.

All the bands are reasonably well reproduced by a single layer model except for the 14.98 μm band. Upon inspection of the peak position, it is obvious that an extra cool ($T \sim 100-200$ K) and optically thin emission component is necessary on top of the warmer component to reproduce the overall band shape. This component is probably the result of the dissociation of water into OH molecules by the interstellar UV field followed by a reaction with CO which could produce CO_2 with a maximum CO_2 abundance of typically 10^{-7} at a few hundred stellar radii where the temperature is of the order of 100 K Willacy & Millar 1997. Moreover, as the hot bands are consecutively shifted to the blue (see Fig. 3) and as these Q-branch transitions (fundamental as well as hot bands) have the highest Einstein A values in the observed wavelength range, it can be expected that this band is optically thick at all wavelengths. The shape of this band will

therefore be the most sensitive to a temperature stratification and the temperature derived for this band with the single-layer model is probably somewhere in between the warmer and the coolest layers. A two-layer model with $T = 100$ K, $N \sim 10^{16}$ and $R \sim$ 100-150 R_* for the second layer is indeed able to reproduce the observed spectrum much better. Also the other derived parameters are probably not very reliable for this band. As the Einstein A coefficients for this band are rather high, one could expect to find the same problem for the fundamental $^{13}CO_2$ bending mode at 15.40 μm even though the $^{13}CO_2$ column density is much lower. This band however is buried in the forest of P-branch lines of the 14.98 μm $^{12}CO_2$ band and therefore this effect is not obvious. Nevertheless the observations clearly show that the CO_2 layer is extended and that the temperature decreases with increasing radius (see Fig. 15).

5.2. Column densities

The derived column densities are $10^{18.5}$ cm^{-2} for all bands except for the 14.98 μm band, where the column density is slightly higher. As discussed in the previous paragraph, this is a consequence of a temperature stratification and the presence of hot bands in the spectrum as well as the presence of a much cooler layer.

5.3. Isotopic ratio

On first sight there is not a single value for the ^{12}C/^{13}C ratio that is compatible with the results derived for the bands individually. However, the problem with the temperature stratification mentioned above will influence the ^{12}C/^{13}C ratio derived for both the 14.98 and 15.40 μm bands and hence the values for these bands are doubtful. The 16.18 μm band on the other hand is rather insensitive for the adopted ^{12}C/^{13}C ratio as can be seen from the uncertainties. As the 13.48 μm band has the lowest optical depth, this would be the best band to derive the ^{12}C/^{13}C ratio. However, this is the weakest band and unfortunately the quality of the spectrum in this region is not too good (see Fig. 10) due to fringe residuals, which hampers a good determination of the ^{12}C/^{13}C ratio. The best guess for the ^{12}C/^{13}C ratio is probably the one derived for the 13.87 μm band which is both very sensitive to the contribution of $^{13}CO_2$ and not too optically thick. We find a ^{12}C/^{13}C ratio value of 10 for this band.

6. Discussion

As mentioned above, the observed peak intensity is a good measure of the radial extent R in our slab models because the bands are optically thick. In fact, R is merely a measure of the emitting *surface* and offers no direct measure of where the CO_2 layer is located. In this section we will assume that each of the CO_2 layers at temperature T is located in a spherical shell around the central star and that $\tau > 1$ for every line of sight that crosses this shell. With these assumptions R is at the same time also a measure for the distance of this shell from the central star. We can then compare the results found for the different bands with temperature and density profiles derived with different models.

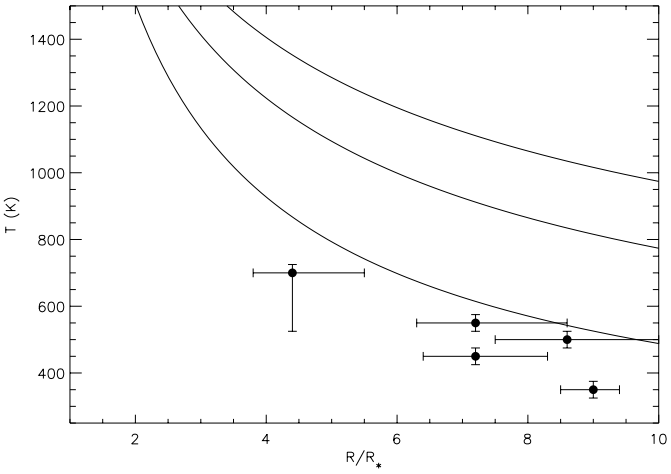

Fig. 15. The filled circles are the temperatures and corresponding radii derived from the observation. The solid lines are temperature profiles with (from top to bottom) α=0.4,0.5,0.7.

6.1. Temperature structure

Bowen (1988) studied heating and cooling of a periodically shocked Mira envelope. The radial kinetic gas temperature variation in the circumstellar shell is represented by a power law

$$T(r) = T_{\rm eff}(r/R_*)^{-\alpha} \quad (17)$$

where the exponent α may range from 0.4 to 0.7. Fig. 15 shows the temperature profile for α =0.4, 0.5 and 0.7 with $T_{\rm eff} = 2447$ K as in our LTE model. Temperature profiles obtained from hydrodynamical atmosphere calculations Höfner & Dorfi 1997 are similar to the $\alpha = 0.7$ profile for the radial distances considered here. The temperatures derived from the CO_2 bands are somewhat lower than expected from these models. This discrepancy may be due to (i) our conversion from R to radial distances, (ii) non-LTE effects or (iii) limitations on the hydrodynamical models.

The first possibility might be true for the 13.48 μm band that still has a relatively low optical depth. We recall that our conversion is based on the assumption that the CO_2 layers are optically thick for every line of sight that crosses it. If this assumption does not hold for the other CO_2 bands, this would imply that a significant part of the CO_2 layer would be transparent and hence we would see emission from the hotter layers inside. Our consistency check described in Sect. 5 assures that this is not the case. Therefore we can rule out this possibility for these bands.

The rotational and vibrational molecular excitation temperatures are the same as the kinetic gas temperature only in LTE. Woitke et al. (1999) calculated vibrational and rotational excitation temperatures for CO_2 in an oxygen-rich dynamical model atmosphere. They find that LTE holds only very close to the central star. Close to the photosphere, the vibrational excitation temperature drops below the kinetic gas temperature. At 2 R_*

also the rotational excitation temperature decouples from the kinetic gas temperature. At 3.5 R_*, the difference between the kinetic gas temperature and the rotational excitation temperature is already more than 300 K, and the discrepancy increases with increasing radius. Our results show a smaller discrepancy (at most 150 K) over a much larger range; moreover the discrepancy does not get larger with increasing radius as would be expected if non-LTE effects are the cause of the differences between our results and the calculated temperature profiles.

We therefore conclude that the hydrodynamical models we compared our results to are not yet adequate to describe the temperature structure of a semiregularly varying AGB star. A new generation of hydrodynmical models that include frequency dependent radiative transfer as described by Höfner 1999 may solve this discrepancy.

6.2. Density structure

From the derived radii R and column densities N we can calculate the number of emitting CO_2 molecules $\mathcal{N}_{\rm CO_2} = N\pi R^2$. To compare this with density laws derived for spherical models, we redistribute this number of molecules into a spherical shell from R_* to R and estimate the average H_2 density in this shell as

$$\bar{n}_{\rm H_2} = \frac{\bar{n}_{\rm CO_2}}{\rm x_{CO_2}} = \frac{1}{\rm x_{CO_2}} \frac{\mathcal{N}_{\rm CO_2}}{\frac{4\pi}{3}(R_{\rm o}^3 - R_*^3)} \tag{18}$$

Note that if we would adopt an inner radius larger than R_*, the average densities would increase. Fig. 16 shows the local H_2 densities calculated from the results in Table 1 adopting a CO_2 abundance of $\rm x_{CO_2}$ = 6 10^{-5}. This is the maximum CO_2 abundance found in the chemical network calculations by Duari et al. (1999). The H_2 densities estimated from our analysis are thus lower limits.

The density structure can also be derived from other observations. Using conservation of mass and assuming a stationary outflow (v=constant), the local H_2 density is given by

$$n_{\rm H_2}(r) = \frac{\dot{M}}{4\pi v(r) r^2 m_{\rm H_2}} \tag{19}$$

To compare this with our estimates, we have to calculate the average density in a spherical shell from R_* to $R_{\rm o}$, or

$$\bar{n}_{\rm H_2} = \frac{\int_{R_*}^{R_{\rm o}} n_{\rm H_2} 4\pi r^2 dr}{\int_{R_*}^{R_{\rm o}} 4\pi r^2 dr} \tag{20}$$

$$= \frac{3\dot{M}}{4\pi v m_{\rm H_2}} \frac{R_{\rm o} - R_*}{R_{\rm o}^3 - R_*^3} \tag{21}$$

Fig. 16 shows the gas density $n_{\rm H_2}(r)$ and the average gas density profile adopting the mass loss rate derived from the broad component in the CO line profile ($\dot{M} = 2.3\ 10^{-7}\ M_\odot/yr$, see Sect. 2) and assuming an outflow velocity in this region of v = 1.5 km/s. Combining the highest mass loss rate with the lowest outflow velocity assures that the derived density profile is an upper limit to the gas densities. For the radii derived from our analysis, this density profile is similar to the results of hydrodynamical model atmosphere calculations Höfner & Dorfi 1997; in these models the density gradient is steeper between R_* and $\sim 3R_*$ and locally there are density enhancements of an order of magnitude due to shocks.

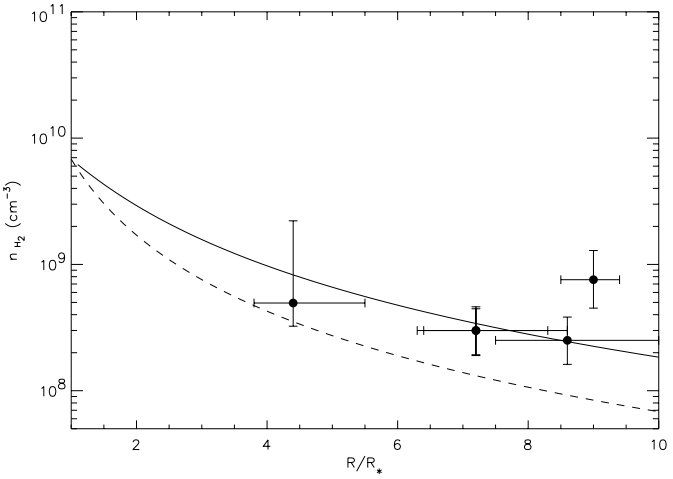

Fig. 16. The local average H_2 gas densities derived from LTE modeling (circles) assuming $\rm x_{CO_2}$= 6 10^{-5}. The dashed line is a density profile and the solid line an average density profile for a stationary outflow assuming v=1.5 km/s and $\dot{M}$=2.3 10^{-7} $M_\odot/yr$.

When comparing the lower limits on the densities derived from the observations with upper limits on the densities from model calculations, we see that both are in reasonable agreement. However, if we take an inner radius for the CO_2 layers that is larger than R_* and adopt a lower CO_2 abundance, the densities derived from our analysis could easily increase an order of magnitude; if on the other hand we would adopt the mass loss rate of 1.7 10^{-8} and/or an outflow velocity of 10 km/s, the theoretical density profile would decrease with an order of magnitude and hence large discrepancies can easily be found. However, recent calculations in which frequency-dependent radiative transfer has been included in an existing hydrodynamics code Höfner (1999) show that the densities can increase dramatically when compared to hydrodynamical models treated in the grey approximation.

The critical density for thermalization of the vibrational bands of CO_2 is of the order of 10^{10} cm^{-3}. The densities derived might be somewhat low for thermalizing the vibrational levels of CO_2; however, as shown in the previous paragraph these densities are only lower limits and could easlily be increased an order of magnitude in which case the gas density is of the order of the critical density.

6.3. Evolutionary status

A good determination of the ^{12}C/^{13}C ratio would allow to pinpoint the location of this AGB star in the HR-diagram; the uncertain value of 10 for the ^{12}C/^{13}C ratio would indicate that no 3^{rd} dredge-up has occurred yet and places this object at the early-AGB, which is supported by the short period and the low mass

loss rate. A firm determination of the $^{12}C/^{13}C$ ratio however requires a multi-layer model.

7. Conclusions

We have developed a simple LTE model for calculating sample spectra for the case of single-layer slab models. We quantitatively compared the model spectra with the SWS observations of EP Aqr for the different CO_2 bands in order to infer the physical properties of the extended atmosphere. The single layer model is able to reproduce on an individual basis the observed band profiles very well even though in some cases the effects of a temperature stratification is discernible in the band profiles. All the bands do show significant optical depth effects.

The parameters derived for the CO_2 bands allow us to estimate the local temperature and density structure of the extended atmosphere. When comparing these results with recent hydrodynamical model atmosphere calculations, it is found that the temperatures are slightly lower while the densities are most likely higher than predicted by these models. Both from the temperature and density structure we conclude that our LTE assumption is justified.

The CO_2 bands are a good probe to study the outer extended atmosphere of AGB stars and the region where dust formation is supposed to take place. Further thermal modeling of other O-rich AGB stars that exhibit these bands is in progress and will be presented in a forthcoming paper.

Acknowledgements. RW and IY acknowledge financial support from an NWO PIONIER grant.

References

Bevington P.R., Robinson D.K., 1992, Data Reduction and Error Analysis for the Physical Sciences. Second edition, McGraw-Hill, New York
Bowen G., 1988, ApJ 329, 299
Cami J., Justtanont K., de Jong T., et al., 1997, In: Heras A.M., Leech K., Trams N.R., Perry M. (eds.) First ISO workshop on Analytical Spectroscopy. ESA-SP419, p. 159
de Graauw T., Haser L., Beintema D., et al., 1996, A&A 315, L49
Dominy J., Wallerstein G., 1987, ApJ 317, 810
Duari D., Cherchneff I., Willacy K., 1999, A&A 341, L47
Engelke C.W., 1992, AJ 104, 1248
González-Alfonso E., Cernicharo J., 1999, In: Cox P., Kessler M.F. (eds.) The Universe as seen by ISO. ESA-SP427, p. 325
Herzberg G., 1945, Infrared and Raman Spectra of Polyatomic Molecules. Van Nostrand, New York
Höfner S., 1999, A&A 346, L9
Höfner S., Dorfi E., 1997, A&A 319, 648
Jura M., Kahane C., 1999, ApJ 521, 302
Justtanont K., Feuchtgruber H., de Jong T., et al., 1998, A&A 330, L17
Kessler M.F., Steinz J., Anderegg M., et al., 1996, A&A 315, L27
Knapp G.R., Young K., Lee E., et al., 1998, ApJS 117, 209
Perryman M., Lindegren L., Kovalevsky J., et al., 1997, A&A 323, L49
Posch T., Kerschbaum F., Mutschke H., et al., 1999, A&A 352, 609
Press W.H., Teukolsky S.A., Vetterling W.T., Flannery B.P., 1992, Numerical Recipes in C: The Art of Scientific Computing. Second edition, Cambridge University Press, New York
Rothman L., Gamache R., Goldman A., et al., 1987, Appl. Opt. 26, 4058
Rothman L.S., Gamache R., Tipping R., et al., 1992, J. Quant. Spectrosc. Radiat. Transfer 48, 469
Rybicki G.B., Lightman A.P., 1979, Radiative Processes in Astrophysics. John Wiley & Sons, Inc., New York
Ryde N., Eriksson K., Gustafsson B., 1999, A&A 341, 579
Ryde N., Eriksson K., Gustafsson B., Lindqvist M., Olofsson H., 1998, Ap&SS 255, 301
Smith V., Lambert D., 1985, ApJ 294, 326
Smith V., Lambert D., 1986, ApJ 311, 843
Sneden C., Pilachowski C., VandenBerg D., 1986, ApJ 311, 826
Tsuji T., Ohnaka K., Aoki W., Yamamura I., 1997, A&A 320, L1
Willacy K., Millar T.J., 1997, A&A 324, 237
Woitke P., Helling C., Winters J., Jeong K., 1999, A&A 348, L17
Yamamura I., de Jong T., Cami J., 1999a, A&A 348, L55
Yamamura I., de Jong T., Onaka T., Cami J., Waters L., 1999b, A&A 341, L9